Hybrid Modeling and Sensitivity Analysis on Reduced Graphene Oxide Field-Effect Transistor

Chao Wang, Haihui Pu, Xiaoyu Sui, Shiyu Zhou , and Junhong Chen

Abstract—The reduced graphene oxide (RGO) field-effect transistor (FET) has been developed and applied in various areas. However, the effective modeling and sensitivity analysis on RGO FET is still a very challenging problem due to the randomness of bandgap and density of states (DOS) in RGO. In this paper, we propose to solve the RGO FET modeling problem by integrating the data-driven thinking and the graphene FET model to develop a hybrid model. The proposed model takes advantages of the similarities between graphene and RGO to generalize the existing graphene FET model, and employs RGO FET drain-current data to characterize the specificity of the model. The basic idea in the proposed model is to modify the graphene DOS to approximate the RGO DOS so that the charge density, mobility and other parameters can be achieved through the approximated RGO DOS. We validate the model accuracy with the RGO FET based sensors that detect chemical concentrations in the aqueous environment. The RGO FET sensitivity analysis is also demonstrated to provide guidance for RGO FET application and manufacturing.

Index Terms—Reduced graphene oxide, field-effect transistor, compact model, sensitivity analysis.

I. INTRODUCTION

RAPHENE is a two-dimensional and one-atom thick carbon sheet with high carrier mobility, high thermal conductivity, and ambipolar transfer characteristics [1]. These intrinsic features make graphene attractive for many electronic applications, e.g., photodetector [2], voltage-tunable modulator [3]. Novoselov *et al.* [4] first demonstrated using graphene as the channel material in field-effect transistors to construct the graphene field-effect transistor (GFET) to achieve high charge density and high conductivity. Over the past few years, the GFET has been significantly studied through experiments and theoretical analysis, and served as sensors, amplifiers and signal mixers in various electronics [5]–[7]. Many compact models [8]–[12]

Manuscript received March 1, 2020; revised June 17, 2020; accepted April 24, 2021. Date of publication April 27, 2021; date of current version May 28, 2021. This work was supported by the National Science Foundation under Grant #1727846. The review of this article was arranged by Associate Editor Prof. Robert W Kelsall. (Corresponding author: Shiyu Zhou.)

Chao Wang is with the Department of Industrial and Systems Engineering, The University of Iowa, Iowa City, IA 52242 USA (e-mail: chao-wang-2@uiowa.edu).

Haihui Pu, Xiaoyu Sui, and Junhong Chen are with the Pritzker School of Molecular Engineering, The University of Chicago, Chicago, IL 60637 USA (e-mail: haihuipu@uchicago.edu; xysui@uchicago.edu; junhongchen@uchicago.edu).

Shiyu Zhou is with the Department of Industrial and Systems Engineering, University of Wisconsin-Madison, Madison, WI 53706 USA (e-mail: szhou@engr.wisc.edu).

Digital Object Identifier 10.1109/TNANO.2021.3076135

have been proposed to quantitatively describe the transfer characteristics in GFET to provide better predictions and analysis of the GFET performance. The sensitivity is a very important performance index of the GFET based system, which characterizes the GFET output (reading) quality in response to various inputs (target change), and further contributes to the system design and production process. The sensitivity analysis [13] is a tool that can quantify such input-output influence and identify the most influential variables to the system uncertainty. In the GFET based sensor, for example, the sensor sensitivity in terms of target changes (temperature, chemical intensity etc.) directly determines the sensor performance, and the sensor sensitivity towards geometrical (sensor dimension) and electrical (carrier density and mobility) features is crucial for senor manufacturing and quality control. The well developed compact models of GFET provide an ideal platform for sensitivity analysis on GFET based system, which results in various experiment and theoretical work in sensitivity analysis on GFET systems [14]. For example, Khan et al. [15] studied the variation propagation in the GFET based inductor-capacitor voltage-controlled oscillators, where the impact of GFET parameters (graphene length, width, mobility and drain-source resistance) variation on the sensitivity of oscillator performance (frequency, phase noise and power dissipation) is statistically analyzed to provide design guidance for the oscillator circuit. Tamersit and Djeffal [16] analyzed the sensitivity of GFET based DNA and gas sensors in response to geometrical and electrical variations of GFET, and the comparison results with other FET based sensors concluded that the GFET based sensor can reach higher sensitivity and specificity on target detection. However, despite the promising properties and potential applications of graphene and GFET, the mass production of graphene without defects or impurities is one of the significant challenges in large-scale application of graphene and related products [17]. The large-area graphene also presents a semimetal behavior posing a critical drawback for digital applications due to the absence of an energy bandgap [18]. In addition, the GFET based chemical detection sensors demonstrated limited detection ability in the aqueous environment, where the sensor requires sensitive reactions between graphene and targeted chemicals [19].

To solve these practical issues, various approaches have been developed to synthesize graphene in an efficient way, such as the micromechanical exfoliation of graphite [4], chemical vapor deposition [20], and the reduction of graphene oxide (GO) [21]. Among these methods, preparation of graphene from GO reduction stands out, because it is promising for the mass production

1536-125X © 2021 IEEE. Personal use is permitted, but republication/redistribution requires IEEE permission. See https://www.ieee.org/publications/rights/index.html for more information.

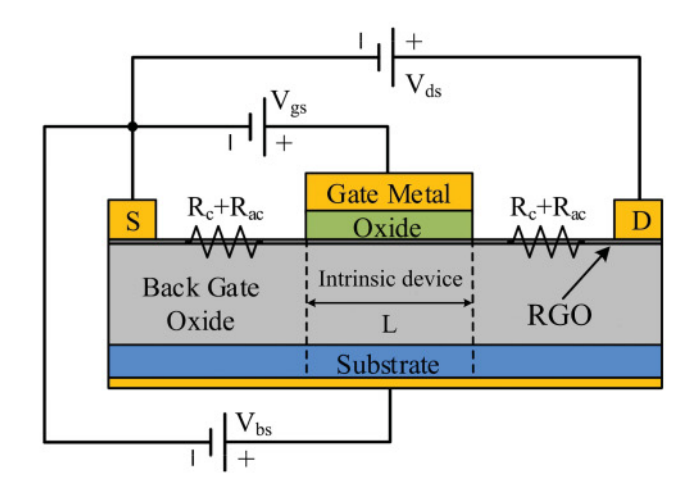


Fig. 1. Cross section of dual-gate RGO FET [9].

of graphene-based materials with tunable energy bandgap [22]. The resulting product, reduced graphene oxide (RGO), resembles graphene but with some residual oxygen. The corresponding FET with RGO as the channel is called reduced graphene oxide FET (RGO FET). A typical dual-gate RGO FET is shown in Fig. 1, where the channel material is monolayer RGO. The V_{qs} is the top-gate voltage, V_{bs} is the back gate voltage, and the V_{ds} is the voltage between external drain (D) and source (S) electrodes. The ground is at the source electrode. The contact and access resistances (R_c and R_{ac}) are considered as one resistance for both source and drain in this paper. The RGO FET has been extensively applied in biological and chemical detection [23], [24]. For example, Chen et al. [19] developed the RGO FET based sensor to detect the mercury ions in aqueous solutions, and the sensor enjoys various merits including wide detection range, quick response and high specificity. Mao et al. [25] demonstrated a specific protein detection biosensor using RGO FET decorated with Au nano-particles, and the experiment results manifested high stability and specificity of sensor performance. Sohn et al. [26] reported the RGO FET based pH sensor and revealed the detection mechanism resulting from the unique functional groups on RGO surface.

Despite the diverse and successful applications of RGO FET, one common issue in existing RGO FET studies is that although the sensitivity is recognized as one of the most important properties of the system, there is few literature comprehensively studying this problem in the RGO FET system. In existing literature, the sensitivity analysis for RGO FET mostly relies on trial and error with different experimental settings, and the analysis results only serve a validation purpose and can hardly provide insights for further improvement of the device. The key difficulty for comprehensive study on RGO FET sensitivity analysis is that there is no compact model quantitatively describing its electrical characteristics. More specifically, unlike the regular atomic structure in graphene, the atomic structure of RGO is still elusive due to its nonstoichiometry. The density of states (DOS) of RGO highly depends on the reduction method/process parameters and the resulting energy bandgap presents a non-linear relationship with the oxygen residual in RGO [27]. The carrier mobility in the RGO also demonstrates complex dependence on the reduction

process and the exact relationship is still unclear [24], [28]. As a result, it is very challenging to develop a physics driven model to characterize the RGO FET, which poses great difficulties for systematic sensitivity analysis of RGO FET based systems.

In this paper, we propose to solve the RGO FET modeling problem by integrating the data-driven thinking and the GFET model to develop a hybrid model. The proposed model takes advantages of the similarities between graphene and RGO to generalize the existing GFET model, at the same time employs RGO FET drain-current data to characterize the specificity of the model. The intuition of the proposed hybrid model is that the RGO can resemble graphene physical and electrical properties by tuning/reducing the oxygen in GO, which indicates the GFET model can also be modified to integrate such tuning process to represent the RGO FET characteristics. Such idea for modeling RGO FET can be found in [29], where a compact RGO FET model for top gate FET was proposed without considering the exist of bandgap. Nevertheless, the direct modification of GFET model based on the reduction physics is too complicated to inspire the RGO FET model. This is because the oxygen reduction process involves various process parameters and the reduction result (atomic structure in RGO) is highly disordered [30]. Alternatively, in our method, we focus on two distinct differences between the RGO and the graphene: bandgap and carrier mobility. We proposed to employ the experiment data from RGO FET to guide the modification of bandgap and carrier mobility in the GFET model. More specifically, the bandgap in graphene is 0 and the carrier mobility can reach 200 000 cm²/(Vs) [31], whereas the RGO has a tunable bandgap associated with the oxygen residual and the carrier mobility is much lower than that in graphene [24]. We treat the bandgap in RGO as an unknown parameter and add it to the DOS of graphene to approximate the DOS of RGO, then the quantum capacitance (an important parameter for RGO FET) is derived based on the approximated DOS of RGO. Under this situation, the RGO FET is treated as a special case of the GFET, where the channel material and circuit characteristics are well represented by the modified DOS. As a result, we can directly plug these modified characteristics into an existing GFET model [9] to achieve the desired RGO FET model, where the bandgap and carrier mobility are unknown parameters. Finally, the RGO FET readings provide the drain-current and the gate voltage data for fitting the model and identifying the unknown parameters. With the fitted model, sensitivity analysis can be performed to demonstrate the RGO FET detection performance and robustness. The contribution of the proposed method is to provide an efficient approximation to the RGO FET model so that the systematic sensitivity analysis can be conducted for the RGO FET based systems. The model performance on I-V curve characterization and sensitivity analysis is validated using a RGO FET based aqueous contaminant (Pb²⁺) detector under various contaminant concentrations. The results demonstrate the effectiveness of the proposed RGO FET model, and the sensitivity analysis identifies the rank of influential process/design parameters in manufacturing the detector.

The rest of the paper is organized as follows: Section II gives the formulation and details about the proposed RGO FET model. The fabrication of the RGO FET sensor is introduced

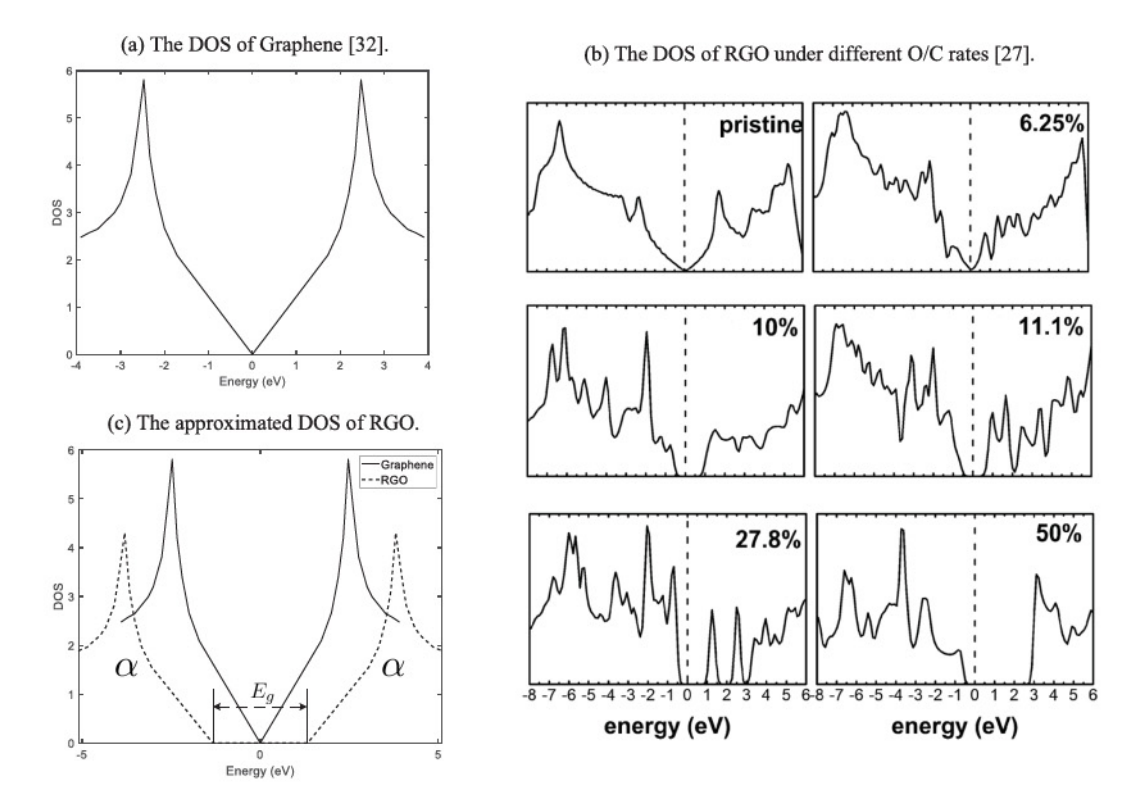


Fig. 2. The DOS of graphene and RGO.

in Section III to provide a test bed for validating the proposed model. Section IV presents the RGO FET model fitting results, and the sensitivity analysis is demonstrated based on the fitted model. Finally, Section V draws conclusion remarks.

II. THE RGO FET MODEL

The goal in this section is to provide an accurate RGO FET drain-current equation for characterizing the sensitivity in the RGO FET system. The proposed model uses tuning parameters, e.g., bandgap, to modify the DOS of graphene to approximate the charge density, quantum capacitance, carrier mobility for the RGO in FET. Then, the electrostatics and drain-current calculation are presented based on the approximations in the RGO FET model to facilitate the model fitting through experiment data. We focus on the monolayer RGO FET in this paper.

A. Model Approximation Basics

The basics and inspiration of approximating the RGO from graphene stems from the physics and electrical similarity (DOS) between RGO and graphene. The DOS of graphene can be well characterized, while the RGO DOS varies according to different reduction processes and is hard to describe quantitatively. Figure 2 (a) and (b) show the graphene DOS and the DOS of RGO under different O/C ratio (oxygen number over carbon number), respectively. Figure 2 (a) is obtained from the analytical expression in [32] for monolayer graphene. Figure 2(b) is the simulation results from [27], where the calculation was done with the Vienna *Ab initio* Simulation Package (VASP) [33] in the frame of the density functional theory [34]. It is clear from Fig. 2 (a) and (b) that the DOS of graphene and low oxygen

rate RGO share very similar structures, which means the charge density in graphene and low oxygen rate RGO should be close to each other. On the other hand, the variational bandgaps and the energy peaks in RGO DOS resulting from the oxygen residual differentiate the RGO with graphene.

The reason we start from graphene is that there are various well developed GFET models originating from the well characterized DOS of graphene. If there is a function that links the DOS of graphene and RGO, we can tactically apply this function to the GFET model to directly achieve the RGO FET model. To approximate this function, we perform transformations of graphene DOS to represent the RGO DOS. The detailed transformation is illustrated in Fig. 2 (c), where the translation of graphene DOS enables the (tunable) bandgap E_a and the scale coefficient α allows more accurate fitting for RGO DOS. We explain the rationality of this transformation in two parts: i) The E_q opens the bandgap for RGO, which is the most distinct difference between graphene and RGO. ii) The α adjusts the shape of the DOS of graphene to approximate the RGO DOS as accurate as possible. It is worth noting that although the adjusted DOS (smooth curve) cannot perfectly match the RGO DOS (with energy peaks), it is the integration of DOS that determines the charge density of RGO (introduced in next section). It is well known that the integration naturally serves as a low pass filter, thus the influence of energy peaks (high frequency disturbance) in RGO DOS is significantly reduced when we consider the integration of the DOS (charge density). As a result, the E_q and α can approximate the RGO DOS to produce an efficient estimation of charge density in RGO. The effects/influence of these two parameters will be propagated into the RGO FET model and be finally optimized using experiment data from the RGO FET.

B. Charge Density and Quantum Capacitance

The electron and hole densities $(n_g \text{ and } p_g)$ in the graphene channel have been derived as [9]

$$\begin{split} n_g &= \int_0^{+\infty} \mathrm{DOS}(E) \cdot f(E) \mathrm{d}E = \frac{2(kT)^2}{\pi (\hbar v_F)^2} \mathfrak{F}_1 \left(\frac{-qV_c}{kT} \right) \\ p_g &= \int_{-\infty}^0 \mathrm{DOS}(E) \cdot (1 - f(E)) \, \mathrm{d}E = \frac{2(kT)^2}{\pi (\hbar v_F)^2} \mathfrak{F}_1 \left(\frac{qV_c}{kT} \right) \end{split}$$

where $\mathrm{DOS}(E)$ is the density of states of graphene, f(E) is the Fermi-Dirac distribution, $\mathfrak{F}_1(\cdot)$ is the first order Fermi-Dirac integral, q is the elementary charge, \hbar represents the reduced Planck constant, v_F is the Fermi velocity in graphene, k is the Boltzmann constant, T is the temperature, and V_c is the channel potential. Based on the DOS transformation in Fig. 2 (c), we can get the electron and hole densities (n and p) in the RGO channel as follows (see the proof in appendix A):

$$n = \int_{0}^{+\infty} DOS_{r}(E) \cdot f(E) dE$$

$$= \alpha \int_{0}^{+\infty} DOS (\mathcal{T}(E)) \cdot f(E) dE$$

$$= \alpha \frac{2(kT)^{2}}{\pi (\hbar v_{F})^{2}} \mathfrak{F}_{1} \left(\frac{-\mathcal{T}(qV_{c})}{kT} \right)$$

$$p = \int_{-\infty}^{0} DOS_{r}(E) \cdot (1 - f(E)) dE$$

$$= \alpha \int_{-\infty}^{0} DOS (\mathcal{T}(E)) \cdot (1 - f(E)) dE$$

$$= \alpha \frac{2(kT)^{2}}{\pi (\hbar v_{F})^{2}} \mathfrak{F}_{1} \left(\frac{\mathcal{T}(qV_{c})}{kT} \right)$$
(2)

where $\mathrm{DOS}_r(E)$ is the approximated DOS of RGO and can be represented as $\mathrm{DOS}_r(E) = \alpha \mathrm{DOS}(\mathcal{T}(E))$. Recall the DOS transformation in Fig. 2 (c), the α gives a scale transformation, and function $\mathcal{T}(\cdot)$ represents the bandgap as follows:

$$\mathcal{T}(x) = \operatorname{sgn}(x) \cdot 1 \left(|x| - \frac{E_g}{2} > 0 \right)$$
$$\cdot \left(|x| - \frac{E_g}{2} \right), \quad x \in (-\infty, +\infty)$$
(3)

where $sgn(\cdot)$ is the sign function and $1(\cdot)$ is the indicator function. We assume the bandgap E_g is centered at 0, but this assumption can be easily relaxed.

According to the n and p in the RGO channel, we can obtain the net mobile sheet charge density as:

$$Q_{net} = q(p - n)$$

$$= \alpha \frac{2q(kT)^2}{\pi(\hbar v_F)^2} \left(\mathfrak{F}_1 \left(\frac{\mathcal{T}(qV_c)}{kT} \right) - \mathfrak{F}_1 \left(\frac{-\mathcal{T}(qV_c)}{kT} \right) \right)$$
(4)

The quantum capacitance C_q describes the intrinsic charge storage of a material excited by a small-signal electric potential [35]. Quantum capacitance is in series with geometric gate capacitance and as C_q is typically small, its high reactance has a significant impact on the overall gate capacitance. The value of quantum capacitance is defined as $C_q = -\partial Q_{net}/\partial V_c$ [36]. The exact form of C_q for graphene [36] cannot be directly used in RGO since the Q_{net} in Eq. 4 is a piece wise function that impairs the C_q smoothness. As a result, we employ the approximation of C_q in graphene [12], [37] and combine it with the function $\mathcal{T}(\cdot)$ to achieve C_q in the RGO:

$$C_q = \alpha \frac{2q^2 |\mathcal{T}(qV_c)|}{\pi (\hbar v_F)^2} \tag{5}$$

The C_q in Eq. 5 will be used in the drain-current calculation in Section II-E.

C. Effective Carrier Mobility

The carrier mobility describes how fast carriers can move through the channel under certain electric field. The application of graphene/RGO FET highly relates with the carrier mobility changes in the channel. For example, the carrier mobility variation upon the adsorption of target chemicals leads to drain-current change [19], [38], [39], which provides the reading/alarm in graphene/RGO FET sensors. The efficient modeling of carrier mobility in RGO would contribute to the drain-current modeling, as well as the sensitivity analysis of RGO FET.

In RGO, the carrier mobility difference between electron and hole is significant [24], which should be considered in the mobility modeling. Tian *et al.* [9] proposed to use an unified model to consider the mobility difference between electron and hole, as well as the mobility dependence on carrier density in graphene. We apply their model to the RGO and obtain the approximation function to represent the effective carrier mobility as follows:

$$\mu_{pn} = h + \frac{14z\mathcal{T}(qV_c)}{q \cdot \sqrt{1 + \left(\frac{\mathcal{T}(qV_c)}{kTln(4)}\right)^2}}$$
 (6)

where $h = (\mu_n + \mu_p)/2$, $z = (\mu_p - \mu_n)$. μ_p and μ_n represent the hole and electron carrier mobility, respectively.

The explicit expression of μ_p and μ_n in Eq. 6 allows the modeling of mobility variation during sensor detection. This provides the possibility for analyzing and comparing the RGO FET sensitivity on target chemical intensity that causes mobility variation. We will demonstrate the sensitivity analysis in Section IV-B.

D. Electrostatics

The analytical results in Eq. 2 and Eqs. 4 to 6 depend on the channel potential V_c . To obtain the channel potential, the equivalent capacitive circuit for RGO FET gate electrostatics is presented in Fig. 3 to provide the channel potential equation.

In Fig. 3, the net voltage at the top gate and the back gate are represented as $V_{gs}^{\prime}=V_{gs}-V_{gs0}$ and $V_{bs}^{\prime}=V_{bs}-V_{bs0}$, respectively. V_{gs} and V_{bs} are the gate voltages applied at the intrinsic terminals, V_{gs0} and V_{bs0} are the constants representing the gate voltages at the point of minimum drain current. The expression

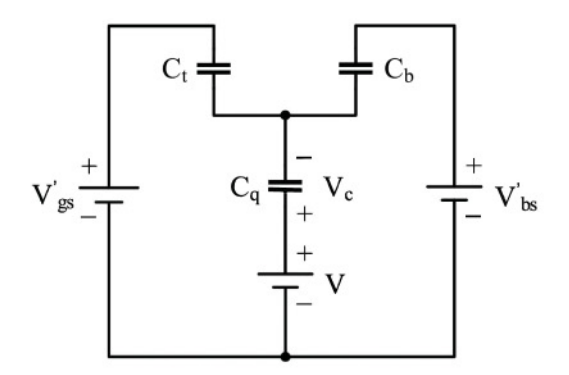


Fig. 3. Equivalent circuit for RGO FET gate electrostatics.

of channel potential can be derived by applying the Kirchhoff's laws to this equivalent circuit as [8]:

$$V_c(C_t + C_b) + Q_{net} + (V'_{ns} - V)C_t + (V'_{hs} - V)C_b = 0$$
(7)

where V is the voltage drop in the RGO channel, C_t and C_b are the top gate and back gate oxide capacitance, respectively. The exact form of Q_{net} is in Eq. 4, which is a function of V_c . The V_c in Eq. 7 can be solved self-consistently using the iterative method introduced in [8]. Please note Eq. 7 is a general equation for electrostatics, which would be flexible for dual gate, top gate and back gate FET. In the real case study in this paper, we will use a back gate FET and the C_t is set to 0 to satisfy the FET gate setting.

E. Drain Current Calculation

In diffusive transport model, the drain current I_{ds} can be written as [40], [41]

$$I_{ds} = \frac{W}{L} \int_{0}^{V_{ds}} \mu_{np} Q_{tot} dV$$
 (8)

where W is the channel width and L is the channel length, V_{ds} is the voltage difference between drain and source, Q_{tot} is the total sheet charge density $Q_{tot} = Q_t + \alpha q n_{pud}$ with n_{pud} the electron-hole puddle [42], and Q_t is the transport sheet charge density $Q_t = q(p+n)$ that can be approximated for RGO as a quadratic form:

$$Q_t = \alpha \frac{2q(kT)^2}{\pi(\hbar v_F)^2} \left(\mathfrak{F}_1 \left(\frac{\mathcal{T}(qV_c)}{kT} \right) + \mathfrak{F}_1 \left(\frac{-\mathcal{T}(qV_c)}{kT} \right) \right)$$

$$\approx \alpha \left(\frac{q\pi(kT)^2}{3(\hbar v_F)^2} + \frac{q\mathcal{T}^2(qV_c)}{\pi(\hbar v_F)^2} \right) \tag{9}$$

To solve the integral in Eq. 8, a variable substitution of V by V_c is needed as the μ_{np} and Q_{tot} are functions of V_c . By deriving Eq. 7 with respect to V_c , we can obtain the relation:

$$\frac{\mathrm{d}V}{\mathrm{d}V_c} = 1 + \frac{C_q}{C_t + C_h} \tag{10}$$

As a result, we combine Eqs. 5, 6, 9 and 10 into Eq. 8, the drain current model can be realized:

$$I_{ds} = \frac{\alpha W}{L} \int_{V_{cs}}^{V_{cd}} \left(\left(\frac{q\pi (kT)^2}{3(\hbar v_F)^2} + \frac{q\mathcal{T}^2 (qV_c)}{\pi (\hbar v_F)^2} \right) + q n_{pud} \right) \cdot$$

$$\left(h + \frac{14z\mathcal{T}(qV_c)}{q \cdot \sqrt{1 + \left(\frac{\mathcal{T}(qV_c)}{kTln(4)}\right)^2}}\right) \cdot \left(1 + \frac{\alpha \frac{2q^2|\mathcal{T}(qV_c)|}{\pi(\hbar v_F)^2}}{C_t + C_b}\right) dV_c$$
(11)

where V_{cs} and V_{cd} are the channel potentials at the source and drain end, respectively, and can be calculated from Eq. 7.

Note that the parameters α , E_g , μ_p , μ_n , n_{pud} in Eq. 11 are unknown and need to be estimated from the drain-current data. After fitting the parameters, the explicit expression of Eq. 11 is a piece wise function that can be obtained through the symbolic calculator. We will discuss the parameter estimation and model fitting in Section IV-A in details.

III. RGO FET SENSOR FABRICATION AND DATA COLLECTION

To validate the proposed model, the RGO FET based water sensor is fabricated to provide drain-current data for model fitting and analysis. We briefly introduce the material preparation and sensor fabrication process, the readers can refer to [43] for more details. First, the single-layer graphene oxide flakes in water dispersion were spin-coated onto a silicon substrate with 285 nm SiO₂ insulation layer, where the metal electrodes contacting individual GO sheet were photolithographically patterned and deposited (5 nm of Ti as adhesion layer followed by 40 nm of Au). Then, the device went through the annealing treatment at 400°C for 5 min in Ar gas to reduce the GO and improve the contact between reduced GO and electrodes. In the sensor surface modification, a 3 nm Al₂ O₃ passivation layer was deposited onto the device surface by atomic-layer deposition (ALD) at 100 °C. To make the sensor recognize the target contamination ions, the isolated and high-density Au nano-particles were sputtered on this Al2 O3 layer as the anchoring sites for probe L-Glutathione reduced (GSH) modification. Finally, the sensing area of the devices were incubated in GSH water solution for 1 h at room temperature, and rinsed with ultrapure water to remove extra GSH. The device would be ready for the sensing test after being dried with compressed air. Please note that the top gate circuit in the fabricated sensor is an open circuit (with single back gate only). In this case, although the Al₂ O₃ is attached on the sensor, we assume its impacts on the V_c (channel potential) is negligible in electrostatics analysis. The influence of this assumption is also demonstrated in Eq. 11, where the effect of C_t can be implicitly replaced by the tuning energy gap α . The V_{cs} and V_{cd} are also influence by the C_t , which can be finally represented by the R_{ac} . As a result, the influence of C_t is implicitly represented by parameters α and R_{ac} in our model. Thus, it is safe to ignore the V_{gs} and top gate oxide capacitance C_t in the model fitting and analysis in single gate RGO FET. This demonstrates that the proposed model is very general to cover both single gate and dual gate RGO FETs.

The lead ion solution with different concentrations were prepared by dissolving Pb^{2+} with ultrapure water. During the test, the FET properties (I_{ds} vs. V_{bs} characteristics) with a fixed drain-source voltage upon different lead ion concentrations were recorded by a Keithley 4200 semiconductor characterization

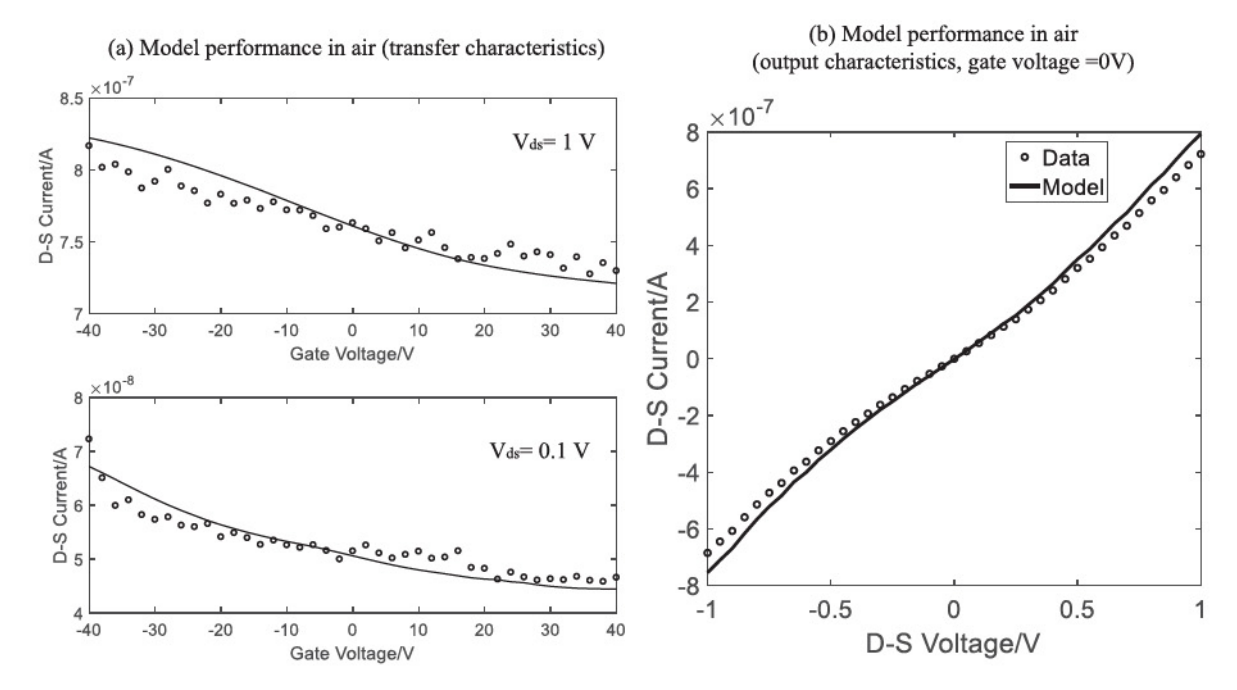


Fig. 4. Model performance for RGO FET sensor in the air (sensor batch 1).

system. To provide a comprehensive view of the sensor performance, we prepare various sets of I_{ds} vs. V_{bs} data in different sensors. The fabricated device and material characterization data (SEM image, Raman spectroscopy, AFM image of the RGO and the Au nanoparticle) are presented in appendix B for readers' information. The I_{ds} vs. V_{bs} data and model analysis would be presented in next section.

IV. MODEL PERFORMANCE AND SENSITIVITY ANALYSIS

A. Model Fitting and Performance

The model in Eq. 11 requires various parameters to evaluate the RGO FET sensor performance. Among these parameters, T, L, W and C_b can be directly obtained, while the α, E_a, μ_p μ_n , V_{bs0} and n_{pud} need to be fitted from the sensor data. Please note the channel materials in the RGO FET sensor contain RGO, Al₂ O₃ and Au nano-particles so the property of the RGO FET sensor might be different with the pure RGO FET containing only RGO as the channel material. In this case, the $DOS_r(E)$ might be influenced by the Al₂ O₃ and Au nano-particles thus cause bias in representing the DOS of RGO. However, our goal in Eq. 11 is to find the optimal representation of n and p to fit the sensor readings. Thus, the bias/influence from the Al₂ O₃ and Au nano-particles will be corrected through the data fitting and parameter tuning. The key idea in modeling the RGO FET sensor using Eq. 11 is to characterize the sensor property/performance by tuning α , E_g , μ_p , μ_n , V_{bs0} and n_{pud} to reflect the attribute changes in RGO FET during sensor fabrication and detection. In this section, we prepare the RGO FET sensors from two manufacturing batches to demonstrate the flexible model fitting and performance on I_{ds} vs. V_{bs} and I_{ds} vs. V_{ds} . The sensitivity analysis on these parameters will also be conducted based on the fitted model.

We first demonstrate the model performance on I_{ds} vs. V_{bs} and I_{ds} vs. V_{ds} curves under different V_{ds} in Fig. 4 and 5, where the data are collected from the single gate RGO FET senor in the air. The corresponding parameters for the RGO FET sensor are shown in Table I and II, where the α , E_g , μ_p , μ_n , V_{bs0} and n_{pud} are fitted through Genetic Algorithms. It can be seen from Fig. 4 and 5 that the proposed model can accurately capture the RGO FET drain-current data under different V_{ds} . The maximum relative error is within 10%.

The sensor is designed to detect the Pb²⁺ in the aqueous environment, and our model can also capture the sensor readings I_{ds} vs. V_{bs} curves in the detection environment. Figure 6 and 7 show the sensor data (circles) in the air and different Pb²⁺ concentrations in two sensors (different with the sensors used in Fig. 4 and 5).

It is obvious that the electrical conductivity decreases as the device Pb2+ concentration increases. This phenomena was observed in other studies and well explained by the charge impurities [44] and external ions (Pb^{2+}) [45]. It can also be observed that the V_{bs0} has a significant decrease (shift left in Fig. 6 and Fig. 7) as the Pb²⁺ solution increases, which is explained by the n-doping effect as the ionic concentration increases [46]. We can also observe the sensor data in the air are different in these two sensors. This is because the humidity in air would influence the sensor readings. In fact, one of the purposes for using ALD deposited Al₂ O₃ on the top of GO channel is to insulate GO from air and diminish the influence from humidity variation. However, the humidity may still affect the statue of the chemical probes. In the fitting, the I_{ds} vs. V_{bs} curve in each sensor are used to fit the parameters, where the E_g , R_{ac} and α are shared by different curves while the V_{bs0} , μ_p , μ_n and n_{pud} are individualized for each curve. The fitted model parameters and other test setting parameters of the two sensors are shown in Table III and Table IV, respectively. Please note that the changes

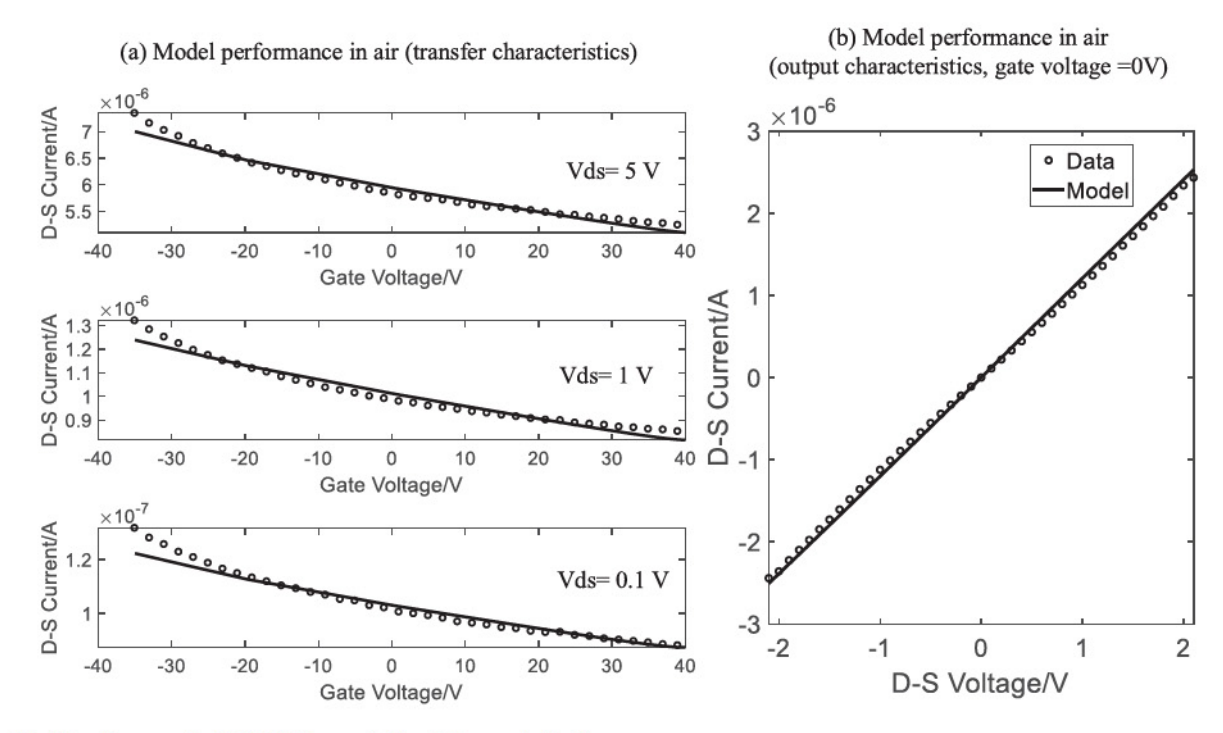


Fig. 5. Model performance for RGO FET sensor in the air (sensor batch 2).

TABLE I PARAMETERS FOR RGO FET SENSOR IN THE AIR (SENSOR BATCH 1)

| Parameters | R_{ac} (k Ω) | T (K) | $L (\mu m)$ | W (μ m) | $V_{bs0}(V)$ | C_b (C/cm ² ·V) |
|------------|--|--|-------------|----------------|------------------------------------|------------------------------|
| Values | 5.7 | 300 | 1.96 | 3.15 | 68 | 1.15×10^{-8} |
| Parameters | $\mu_p \text{ (cm}^2/\text{V}\cdot\text{s)}$ | $\mu_n \text{ (cm}^2/\text{V}\cdot\text{s)}$ | α | E_g (eV) | $n_{pud} \text{ (cm}^{-2}\text{)}$ | |
| Values | 0.27 | 0.07 | 0.12 | 2.06 | 0.070×10^{12} | |

TABLE II
PARAMETERS FOR RGO FET SENSOR IN THE AIR (SENSOR BATCH 2)

| Parameters | R_{ac} (k Ω) | T (K) | $L (\mu m)$ | W (μm) | $V_{bs0}(V)$ | C_b (C/cm ² ·V) |
|------------|--|--|-------------|------------|------------------------------------|------------------------------|
| Values | 5.2 | 300 | 2.89 | 2.07 | 52 | 1.15×10^{-8} |
| Parameters | $\mu_p \text{ (cm}^2/\text{V}\cdot\text{s)}$ | $\mu_n \text{ (cm}^2/\text{V}\cdot\text{s)}$ | α | E_g (eV) | $n_{pud} \text{ (cm}^{-2}\text{)}$ | |
| Values | 0.95 | 0.05 | 0.14 | 1.95 | 0.066×10^{12} | |

TABLE III
PARAMETERS FOR RGO FET SENSOR IN DETECTION (SENSOR BATCH 1)

| | Air | Water | 10ppb | 20ppb | | | |
|--|-------|-------|------------------|--------|--|--|--|
| V_{bs0} (V) | 57 | 44 | 27 | 14 | | | |
| $\mu_p \text{ (cm}^2/\text{V}\cdot\text{s)}$ | 1.78 | 2.70 | 2.12 | 2.38 | | | |
| $\mu_n \text{ (cm}^2/\text{V}\cdot\text{s)}$ | 0.11 | 0.21 | 0.41 | 0.67 | | | |
| $n_{pud} \ (10^{12} \text{cm}^{-2})$ | 0.114 | 0.096 | 0.0890 | 0.0915 | | | |
| R_{ac} (k Ω) | 3.4 | | | | | | |
| T (K) | 300 | | | | | | |
| W (μm) | | 3 | .30 | | | | |
| $L(\mu m)$ | | 1 | .93 | | | | |
| C_b (C/cm ² ·V) | | 1.15 | $\times 10^{-8}$ | | | | |
| α | 0.22 | | | | | | |
| E_g (eV) | | 1 | .55 | | | | |
| $V_{ds}(V)$ | 1 | | | | | | |

in the n_{pud} , V_{bs0} , μ_p and μ_n are very complicated compensation processes for various external and internal changes, e.g., ions/impurities, relative permittivity and the conductance, due to the sensing environment change. As a result, the n_{pud} , V_{bs0} , μ_p and μ_n serve the hybrid role in representing the physical information and compensating for environment changes. The model performance for each detection scenario is shown in Fig. 6 and Fig. 7 with solid curves, where the proposed model can accurately capture the RGO FET sensor readings. It can also be observed from Fig. 6 that the type of the device changes from p type to ambipolar, which is consistent with the n-doping effect that causes the shift of the Dirac point. This also demonstrates that our model can characterize ambipolar features in the sensor data. As a result, the model performance in device detection environment also validates the model effectiveness. We also want to point out that comparing Fig. 4 (a) with Fig. 6 (and Fig. 5 (a) with Fig. 7), the fitting/modeling performance, especially in

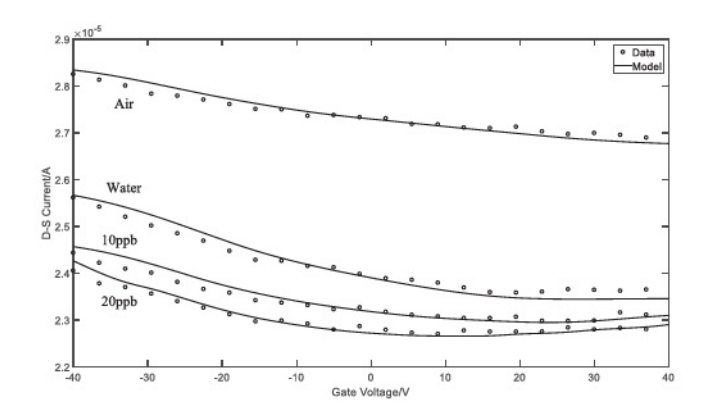


Fig. 6. Model performance for RGO FET sensor in detection (sensor batch 1).

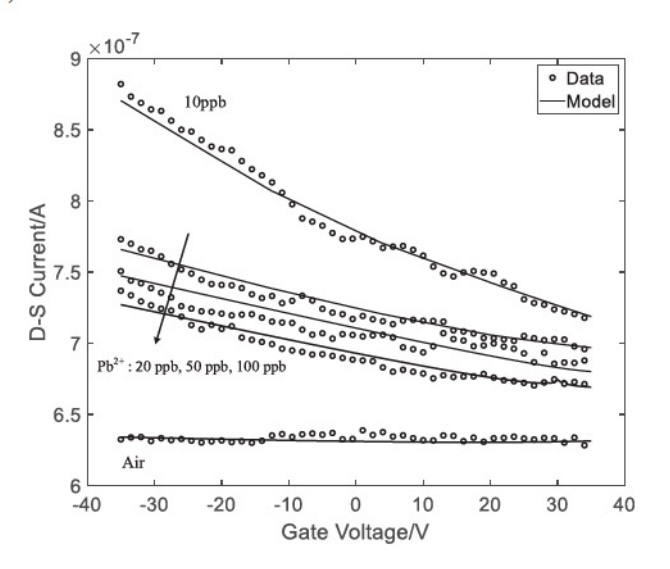


Fig. 7. Model performance for RGO FET sensor in detection (sensor batch 2).

TABLE IV PARAMETERS FOR RGO FET SENSOR IN DETECTION (SENSOR BATCH 2)

| | Air | 10ppb | 20ppb | 50ppb | 100ppb | | |
|---|-------|-------|---------|-------|--------|--|--|
| V_{bs0} (V) | 48 | 47 | 45 | 38 | 30 | | |
| $\mu_p \ (\text{cm}^2/\text{V}\cdot\text{s})$ | 0.02 | 0.11 | 0.08 | 0.07 | 0.07 | | |
| $\mu_n \text{ (cm}^2/\text{V}\cdot\text{s)}$ | 0.001 | 0.06 | 0.05 | 0.05 | 0.04 | | |
| $n_{pud} \ (10^{12} \text{cm}^{-2})$ | 0.121 | 0.071 | 0.077 | 0.081 | 0.083 | | |
| R_{ac} (k Ω) | | | 5.3 | | | | |
| T (K) | | | 300 | | | | |
| $W (\mu m)$ | 3.07 | | | | | | |
| $L(\mu m)$ | 1.01 | | | | | | |
| C_b (C/cm ² ·V) | | | 1.15×10 | -8 | | | |
| α | | | 0.2 | | | | |
| E_g (eV) | 2.27 | | | | | | |
| $V_{ds}(V)$ | | | 1 | | | | |

 $V_{bs} \in (-40 \, \mathrm{V}, -20 \, \mathrm{V})$ of Fig. 4/5 (a) is slightly worse than that in Fig. 6/7. One possible explanation of the fitting performance difference is the model assumption in parameter flexibility. For example, in Fig. 5 (a), the model is assumed to have the same parameters, e.g., carrier mobility, for different V_{ds} values in the air. This is motivated by the RGO physics [27]. While in the Fig. 7, some parameters, e.g., carrier mobility and V_{bs0} , are customized for each contamination scenario. This is also

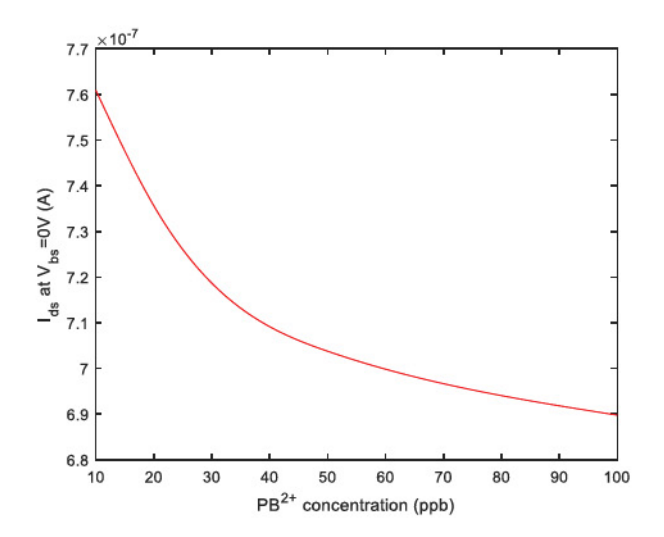


Fig. 8. Senor performance and detection range (sensor batch 2).

supported by the fact that the contamination will potentially change the RGO FET physics properties [44], [45]. In this case, the fitting in Fig. 7 has more flexibility than that in Fig. 5 (a), which results in a slightly better performance in Fig. 7.

To demonstrate the sensor detection limit and linear range, we also provide a calibration curve for the sensors in batch 2 in Fig. 8, where we use the I_{ds} at $V_{bs}=0\ V$ to evaluate the sensor performance. We can see the sensor performs linearly between 10-40 ppb, the curve starts to saturate around concentration 60 ppb.

B. Sensitivity Analysis

The sensitivity analysis studies how the uncertainty in the output of a complex system can be apportioned to different source of uncertainty in its inputs. In the RGO FET based system, the drain-current is the system/sensor output, and the inputs involve various parameters. These input parameters can influence the system performance from different aspects, e.g., manufacturing (W, L, C_b) , detection $(\mu_n, \mu_p, V_{bs0}, E_g)$ and working condition (T). The sensitivity analysis on these parameters could provide insights and guidance for RGO FET application and manufacturing.

In this section, we will employ the variance-based sensitivity analysis (Sobol method) [47] to quantify the input-output influence and identify the most influential parameters to the system uncertainty. The Sobol method treats the output Y as a function of various independent inputs $X = \{X_1, \ldots, X_d\}$ (Y = g(X)) and decomposes the variance of the output as follows:

$$Var(Y) = \sum_{i=1}^{d} V_i + \sum_{i < j}^{d} V_{ij} + \dots + V_{12 \dots d}$$
 (12)

where $V_i = \operatorname{Var}_{X_i}(E_{\mathbf{X}_{\sim i}}(Y|X_i)),$ $V_{ij} = \operatorname{Var}_{X_{ij}}(E_{\mathbf{X}_{\sim ij}}(Y|X_i,X_j)) - V_i - V_j.$ The $X_{\sim i}$ represents the set of all variables except X_i . The variance decomposition in Eq. 12 shows how the variance of the model output can be decomposed into terms attributed to each input, as well as the interaction effects between them.

| | | W | L | μ_p | μ_n | C_{b} | V_{bs0} | E_{g} |
|-------|-------|--------|--------|---------|---------|---------|-----------|---------|
| Air | S_i | 0.3937 | 0.3162 | 0.1198 | 0.0623 | 0.0547 | 0.0501 | 0.0032 |
| | Rank | 1 | 2 | 3 | 4 | 5 | 6 | 7 |
| Water | S_i | 0.3898 | 0.3160 | 0.1086 | 0.0246 | 0.0105 | 0.0103 | 0.0002 |
| water | Rank | 1 | 2 | 3 | 4 | 5 | 6 | 7 |
| 10ppb | S_i | 0.3931 | 0.3885 | 0.1140 | 0.0840 | 0.0100 | 0.0102 | 0.0002 |
| | Rank | 1 | 2 | 3 | 4 | 6 | 5 | 7 |
| 20ppb | S_i | 0.3809 | 0.3725 | 0.1293 | 0.0967 | 0.0103 | 0.0101 | 0.0002 |
| | Rank | 1 | 2 | 3 | 4 | 5 | 6 | 7 |

TABLE V
SENSITIVITY ANALYSIS FOR RGO FET BASED SENSOR (SENSOR BATCH 1)

TABLE VI SENSITIVITY ANALYSIS FOR RGO FET BASED SENSOR (SENSOR BATCH 2)

| | | W | L | μ_p | μ_n | C_b | V_{bs0} | E_g |
|--------|-------|--------|--------|---------|---------|--------|-----------|--------|
| Air | S_i | 0.3493 | 0.3314 | 0.1628 | 0.1031 | 0.0106 | 0.0208 | 0.0220 |
| All | Rank | 1 | 2 | 3 | 4 | 7 | 6 | 5 |
| 10ppb | S_i | 0.3196 | 0.3141 | 0.1437 | 0.1102 | 0.0350 | 0.0335 | 0.0439 |
| торро | Rank | 1 | 2 | 3 | 4 | 6 | 7 | 5 |
| 20ppb | S_i | 0.3276 | 0.3110 | 0.1684 | 0.1128 | 0.0244 | 0.0220 | 0.0338 |
| Zoppo | Rank | 1 | 2 | 3 | 4 | 6 | 7 | 5 |
| 50ppb | S_i | 0.3006 | 0.3125 | 0.1768 | 0.1230 | 0.0253 | 0.0275 | 0.0343 |
| | Rank | 2 | 1 | 3 | 4 | 7 | 6 | 5 |
| 100ppb | S_i | 0.3035 | 0.3129 | 0.1892 | 0.1241 | 0.0200 | 0.0164 | 0.0339 |
| | Rank | 2 | 1 | 3 | 4 | 6 | 7 | 5 |

A widely used variance-based measure of sensitivity is called the first-order sensitivity index [48]:

$$S_i = \frac{V_i}{\text{Var}(Y)} \tag{13}$$

Equation 13 is the contribution to the output variance of the main effect of X_i , which will be used in our sensitivity analysis for each input parameter. More specifically, we will study the drain-current sensitivity to the input parameters W, L, V_{bs0} , C_b , E_g , μ_p and μ_n . Please note that we do not include T into consideration because the T is associated with μ_p and μ_n , which violates the independent inputs assumption in Sobol method. The readers can refer to [24] for studies on temperature influence on the RGO performance. In our sensitivity analysis, we choose the drain-current readings when $V_{bs}=0$ V as the output since these are the readings demonstrated on the sensor device. We use the parameters in Table III and IV as the initial inputs, then the values of W, L, C_b , E_g , V_{bs0} , μ_p and μ_n are allowed to shift $\pm 10\%$ around their initial values to obtain the first-order sensitivity index through numerical method [47].

Since we obtained the fitted model in Section IV-A, the sensitivity index can be evaluated in an efficient way. The results for two sensors in Fig. 6 and 7 are shown in Table V and VI, respectively. It can be seen from the Table V and VI that although the sensitivity index values change across different scenarios, the rank of the sensitivity index almost keeps the same. From the two tables, we can see there are three groups of these parameters in terms of the sensitivity. The first group contains the FET channel width W and length L, which are recognized as the most influential parameters to the sensor readings. This reveals the importance of dimension control in producing the RGO FET based

sensors since the small manufacturing deviation from nominal dimensions would result in large shifts from the calibrated readings. The sensitivity of carrier mobility (μ_p and μ_n) ranks after the dimension, which is reasonable and desirable since the carrier mobility is a direct reflection of chemical concentration. We can also observe that the sensitivity index values of the carrier mobility become larger when Pb2+ increases, which indicates that the sensor becomes more sensitive in detecting higher contamination. The last group includes the C_b , V_{bs0} and E_g . The C_b is mainly influenced by the gate material (relative permittivity) and the dimension of the back gate. Since the gate material is usually well controlled, the low sensitivity of the C_b indicates the drain current readings are robust towards the gate dimension. This is a desirable feature since the gate dimension might be different among sensors, and the robustness of C_b is fundamental to the stable sensor readings. The sensitivity of E_q accounts for the influence of RGO FET fabrication process on the sensor readings. This influence is also expected to be as small as possible since the RGO layer may interact with other materials during the sensor fabrication process. The low sensitivity of E_q indicates the DOS modeling is robust towards the interactions between RGO and other materials. The low sensitivity of V_{bs0} can be explained by the large estimated V_{bs0} values, which make the influence of V_{bs0} very small at the $V_{bs} = 0$ V position.

V. CONCLUSION

In this paper, we present a RGO FET compact model suitable for drain-current modeling and circuit/sensor sensitivity analysis. The basic idea in the proposed model is to modify

the graphene DOS to approximate the RGO DOS so that the charge density, mobility and other parameters can be achieved through the approximated RGO DOS. The proposed model enables closed-form analytical solutions for the drain-current readings of the RGO FET. We validate the accuracy of the model performance with the RGO FET based Pb2+ sensor that detects the concentration of Pb2+ in the aqueous environment. The results demonstrate the model can capture the sensor drain-current readings in both air and aqueous environment. The sensitivity analysis is also performed in terms of carrier mobility (ionic concentration), sensor size and other parameters in the RGO FET. The sensitivity analysis results show the sensor size (width and length) is the most influential parameter to the sensor reading, which indicates the importance of dimension control for sensor fabrication in the future. The sensitivity analysis also reveals that the sensor performance is highly sensitive to the effective charge mobility, especially in the aqueous detection environment. This further provides insights for achieving better response of the sensor by calibrating the sensor in aqueous rather than air environment.

Some interesting open issues remain in the proposed method. First, the quantum capacitance in the proposed method is proportional to the channel potential, which will cause errors in modeling the net mobile sheet charge density when $q|V_c| \ll kT$. A classic way to solve this problem in GFET model is to employ quadratic relationship between the quantum capacitance and the channel potential. However, this method cannot fit the situation in RGO FET since the bandgap in RGO makes the net mobile sheet charge density zero when $q|V_c| \ll kT$, which means the quantum capacitance will not be a continuous function of the channel potential. One potential solution to this problem is to assume the n_{pud} changes with the channel potential and the sheet charge density resulting from n_{pud} can be used to compensate for the step change in the quantum capacitance. Another issue we have in the method is the offline parameter fitting that is time consuming. The main reason is that it is very challenging to construct an efficient objective function to evaluate the parameters due to complex relationship among these parameters. One potential way to solve this problem is to resort to the distributed estimation to improve the convergence rate and efficiency in the parameter estimation. We would study these interesting problems in the future.

APPENDIX

A. Proof of Eq. 2

We show the proof sketch for n as follows:

$$\begin{split} n &= \int_0^{+\infty} \mathrm{DOS}_r(E) \cdot f(E) \mathrm{d}E \\ &= \alpha \int_{E_g/2}^{+\infty} \mathrm{DOS}(E - E_g/2) \cdot f(E) \mathrm{d}E \\ &= \alpha \int_{E_g/2}^{+\infty} \mathrm{DOS}(E - E_g/2) \cdot (1 + \mathrm{exp}[(E - E_F)/kT])^{-1} \, \mathrm{d}E \\ &= \alpha \int_{E_g/2}^{+\infty} \mathrm{DOS}(E - E_g/2) \cdot \end{split}$$

$$(1 + \exp[(E - E_g/2 - (E_F - E_g/2))/kT])^{-1} dE$$

$$= \alpha \int_0^{+\infty} DOS(E') \cdot (1 + \exp[(E' - (E'_f))/kT])^{-1} dE'$$
(14)

where $E'=E-E_g/2$ and $E'_f=E_F-E_g/2$. Please also note that $E_F=qV_c$ and the relationship between Eqs. 14 and 1, then Eq. 14 becomes

$$n = \alpha \frac{2(kT)^2}{\pi(\hbar v_F)^2} \mathfrak{F}_1 \left(-\frac{(qV_c - E_g/2)}{kT} \right)$$
 (15)

Also note that the $qV_c-E_g/2$ can only take effect when $|qV_c|>E_g/2$ because of the energy bandgap, which results in

$$n = \alpha \frac{2(kT)^2}{\pi(\hbar v_F)^2} \mathfrak{F}_1\left(\frac{-\mathcal{T}(qV_c)}{kT}\right)$$
 (16)

B. Device and Material Characterization



Fig. 9. Fabricated sensor.

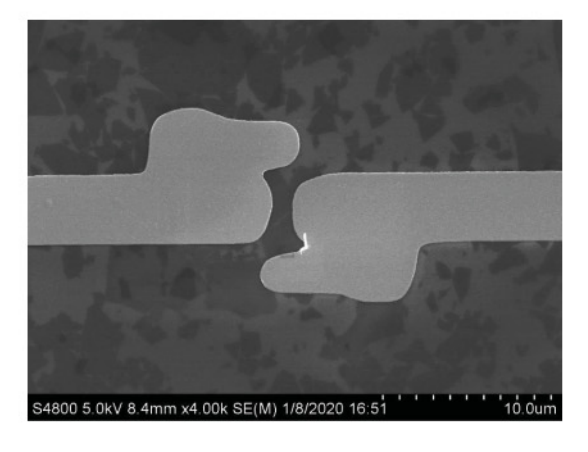


Fig. 10. SEM of the sensing channel (shaded parts are GO flakes).

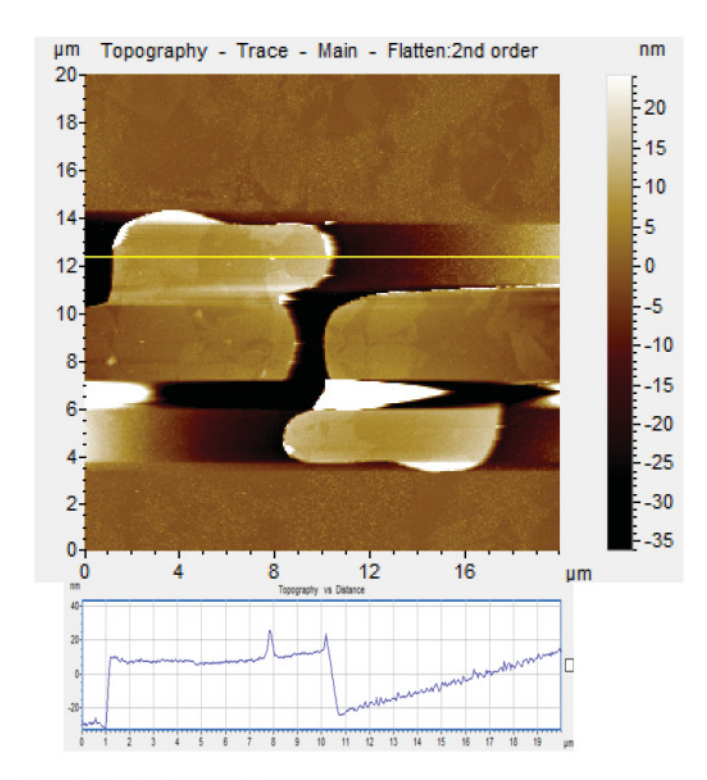


Fig. 11. AFM of the device.

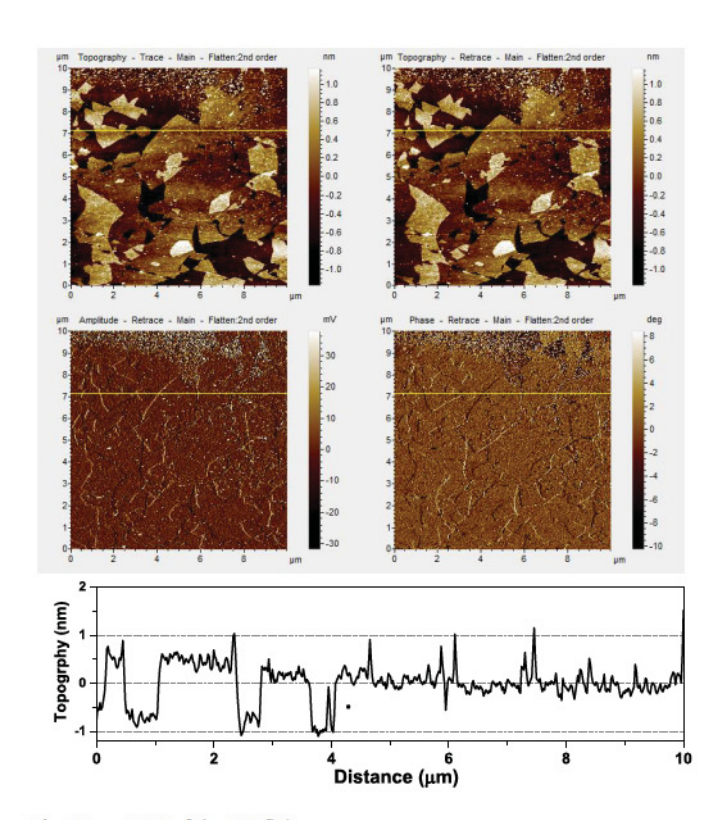


Fig. 12. AFM of the GO flake.

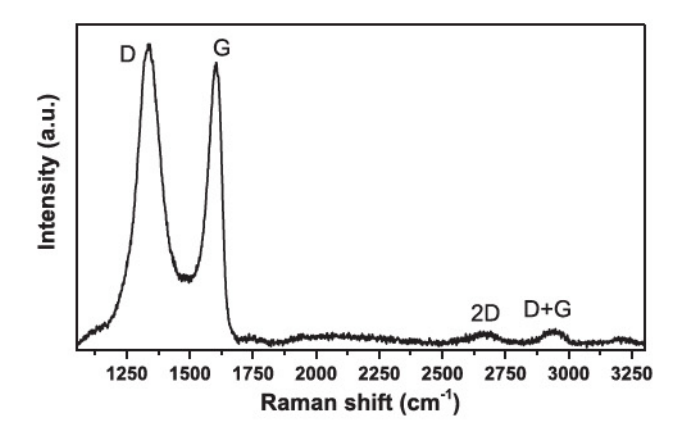


Fig. 13. Raman spectroscopy of the GO with D and G bands.

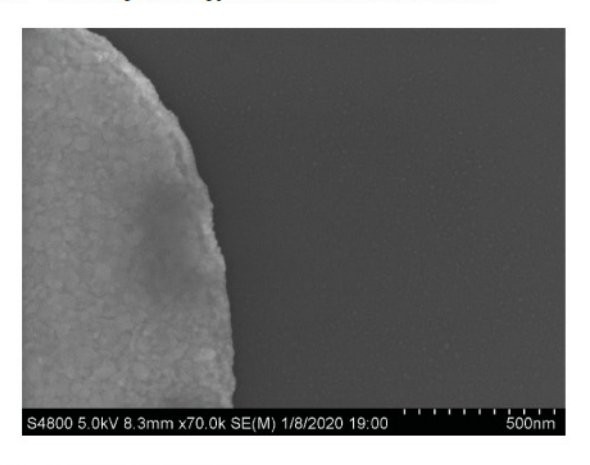


Fig. 14. SEM of the Au particle.

REFERENCES

- A. K. Geim, "Graphene: Status and prospects," Science, vol. 324, no. 5934, pp. 1530–1534, 2009.
- [2] C.-H. Liu, Y.-C. Chang, T. B. Norris, and Z. Zhong, "Graphene photodetectors with ultra-broadband and high responsivity at room temperature," *Nat. Nanotechnol.*, vol. 9, no. 4, 2014, Art. no. 273.
- [3] B. Sensale-Rodriguez et al., "Broadband graphene terahertz modulators enabled by intraband transitions," Nat. Commun., vol. 3, 2012, Art. no. 780.
- [4] K. S. Novoselov et al., "Electric field effect in atomically thin carbon films," Science, vol. 306, no. 5696, pp. 666–669, 2004.
- [5] H. Wang, D. Nezich, J. Kong, and T. Palacios, "Graphene frequency multipliers," *IEEE Electron Device Lett.*, vol. 30, no. 5, pp. 547–549, May 2009.
- [6] M. E. Ramón et al., "Three-Gigahertz graphene frequency doubler on quartz operating beyond the transit frequency," *IEEE Trans. Nanotechnol.*, vol. 11, no. 5, pp. 877–883, Sep. 2012.
- [7] X. Yang, G. Liu, A. A. Balandin, and K. Mohanram, "Triple-mode single-transistor graphene amplifier and its applications," ACS Nano, vol. 4, no. 10, pp. 5532–5538, 2010.
- [8] G. M. Landauer, D. Jiménez, and J. L. González, "An accurate and veriloga compatible compact model for graphene field-effect transistors," *IEEE Trans. Nanotechnol.*, vol. 13, no. 5, pp. 895–904, Sep. 2014.
- [9] J. Tian, A. Katsounaros, D. Smith, and Y. Hao, "Graphene field-effect transistor model with improved carrier mobility analysis," *IEEE Trans. Electron Devices*, vol. 62, no. 10, pp. 3433–3440, Oct. 2015.

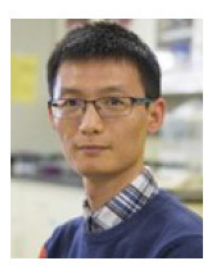
- [10] J.-D. Aguirre-Morales, S. Frégonése, C. Mukherjee, C. Maneux, and T. Zimmer, "An accurate physics-based compact model for dual-gate bilayer graphene FETs," *IEEE Trans. Electron Devices*, vol. 62, no. 12, pp. 4333–4339, Dec. 2015.
- [11] H. Wang, A. Hsu, J. Kong, D. A. Antoniadis, and T. Palacios, "Compact virtual-source current-voltage model for top-and back-gated graphene field-effect transistors," *IEEE Trans. Electron Devices*, vol. 58, no. 5, pp. 1523–1533, May 2011.
- [12] D. Jimenez and O. Moldovan, "Explicit drain-current model of graphene field-effect transistors targeting analog and radio-frequency applications," *IEEE Trans. Electron Devices*, vol. 58, no. 11, pp. 4049–4052, Nov. 2011.
- [13] A. Saltelli, S. Tarantola, F. Campolongo, and M. Ratto, "Sensitivity analysis in practice: a guide to assessing scientific models," New York: Wiley, 2004.
- [14] T. Kuila, S. Bose, P. Khanra, A. K. Mishra, N. H. Kim, and J. H. Lee, "Recent advances in graphene-based biosensors," *Biosensors Bioelectron.*, vol. 26, no. 12, pp. 4637–4648, 2011.
- [15] M. A. Khan, S. P. Mohanty, and E. Kougianos, "Statistical process variation analysis of a graphene FET based LC-VCO for wlan applications," in *Proc.* 15th Int. Symp. Qual. Electron. Des., 2014, pp. 569–574.
- [16] K. Tamersit and F. Djeffal, "Double-gate graphene nanoribbon field-effect transistor for DNA and gas sensing applications: Simulation study and sensitivity analysis," *IEEE Sensors J.*, vol. 16, no. 11, pp. 4180–4191, Jun. 2016.
- [17] C. H. A. Wong, Z. Sofer, M. Kubešová, J. Kučera, S. Matějková, and M. Pumera, "Synthetic routes contaminate graphene materials with a whole spectrum of unanticipated metallic elements," *Nat. Acad. Sci.*, vol. 111, no. 38, pp. 13774–13779, 2014.
- [18] H. Zhang, "Ultrathin two-dimensional nanomaterials," ACS Nano, vol. 9, no. 10, pp. 9451–9469, 2015.
- [19] K. Chen et al., "Hg (II) ion detection using thermally reduced graphene oxide decorated with functionalized gold nanoparticles," Anal. Chem., vol. 84, no. 9, pp. 4057–4062, 2012.
- [20] Y. Huang, X. Dong, Y. Shi, C. M. Li, L.-J. Li, and P. Chen, "Nanoelectronic biosensors based on CVD grown graphene," *Nanoscale*, vol. 2, no. 8, pp. 1485–1488, 2010.
- [21] I. K. Moon, J. Lee, R. S. Ruoff, and H. Lee, "Reduced graphene oxide by chemical graphitization," *Nat. Commun.*, vol. 1, no. 1, pp. 73–78, 2010.
- [22] S. Mao, H. Pu, and J. Chen, "Graphene oxide and its reduction: modeling and experimental progress," Rsc Adv., vol. 2, no. 7, pp. 2643–2662, 2012.
- [23] H. G. Sudibya, Q. He, H. Zhang, and P. Chen, "Electrical detection of metal ions using field-effect transistors based on micropatterned reduced graphene oxide films," ACS Nano, vol. 5, no. 3, pp. 1990–1994, 2011.
- [24] C. Gómez-Navarro et al., "Electronic transport properties of individual chemically reduced graphene oxide sheets," Nano Lett., vol. 7, no. 11, pp. 3499–3503, 2007.
- [25] S. Mao, G. Lu, K. Yu, Z. Bo, and J. Chen, "Specific protein detection using thermally reduced graphene oxide sheet decorated with gold nanoparticleantibody conjugates," Adv. Mater., vol. 22, no. 32, pp. 3521–3526, 2010.
- [26] I.-Y. Sohn et al., "ph sensing characteristics and biosensing application of solution-gated reduced graphene oxide field-effect transistors," Biosensors Bioelectron., vol. 45, pp. 70–76, 2013.
- [27] H. Huang, Z. Li, J. She, and W. Wang, "Oxygen density dependent band gap of reduced graphene oxide," J. Appl. Phys., vol. 111, no. 5, 2012, Art. no. 054317.
- [28] C.-Y. Su et al., "Electrical and spectroscopic characterizations of ultralarge reduced graphene oxide monolayers," Chem. Mater., vol. 21, no. 23, pp. 5674–5680, 2009.
- [29] K. Vasu, B. Chakraborty, S. Sampath, and A. Sood, "Probing top-gated field effect transistor of reduced graphene oxide monolayer made by dielectrophoresis," *Solid State Commun.*, vol. 150, no. 29-30, pp. 1295–1298, 2010.
- [30] A. Nourbakhsh et al., "Bandgap opening in oxygen plasma-treated graphene," Nanotechnol., vol. 21, no. 43, 2010, Art. no. 435203.
- [31] K. I. Bolotin et al., "Ultrahigh electron mobility in suspended graphene," Solid State Commun., vol. 146, no. 9/10, pp. 351–355, 2008.
- [32] A. Rozhkov, A. Sboychakov, A. Rakhmanov, and F. Nori, "Electronic properties of graphene-based bilayer systems," *Phys. Rep.*, vol. 648, pp. 1–104, 2016.
- [33] G. Kresse and J. Furthmüller, "Efficiency of ab-initio total energy calculations for metals and semiconductors using a plane-wave basis set," *Comput. Mater. Sci.*, vol. 6, no. 1, pp. 15–50, 1996.
- [34] W. Kohn and L. J. Sham, "Self-consistent equations including exchange and correlation effects," *Phys. Rev.*, vol. 140, no. 4A, 1965, Paper A 1133.

- [35] H.-S. P. Wong and D. Akinwande, Carbon Nanotube and Graphene Device Physics. Cambridge, U.K.: Cambridge University Press, 2011.
- [36] T. Fang, A. Konar, H. Xing, and D. Jena, "Carrier statistics and quantum capacitance of graphene sheets and ribbons," *Appl. Phys. Lett.*, vol. 91, no. 9, 2007, Art. no. 092109.
- [37] S. Thiele, J. Schaefer, and F. Schwierz, "Modeling of graphene metal-oxide-semiconductor field-effect transistors with gapless largearea graphene channels," J. Appl. Phys., vol. 107, no. 9, 2010, Art. no. 094505.
- [38] F. Schedin et al., "Detection of individual gas molecules adsorbed on graphene," Nat. Mater., vol. 6, no. 9, 2007, Art. no. 652.
- [39] Y. Dan, Y. Lu, N. J. Kybert, Z. Luo, and A. C. Johnson, "Intrinsic response of graphene vapor sensors," *Nano Lett.*, vol. 9, no. 4, pp. 1472–1475, 2009.
- [40] B. Chakraborty, A. Das, and A. Sood, "The formation of a p-n junction in a polymer electrolyte top-gated bilayer graphene transistor," *Nanotechnol.*, vol. 20, no. 36, 2009, Art. no. 365203.
- [41] I. Meric, M. Y. Han, A. F. Young, B. Ozyilmaz, P. Kim, and K. L. Shepard, "Current saturation in zero-bandgap, top-gated graphene field-effect transistors," *Nat. Nanotechnol.*, vol. 3, no. 11, 2008, Art. no. 654.
- [42] W. Zhu, V. Perebeinos, M. Freitag, and P. Avouris, "Carrier scattering, mobilities, electrostatic potential in monolayer, bilayer, and trilayer graphene," *Phys. Rev. B*, vol. 80, no. 23, 2009, Art. no. 235402.
- [43] A. Maity et al., "Pulse-driven capacitive lead ion detection with reduced graphene oxide field-effect transistor integrated with an analyzing device for rapid water quality monitoring," ACS Sensors, vol. 2, no. 11, pp. 1653–1661, 2017.
- [44] F. Chen, J. Xia, and N. Tao, "Ionic screening of charged-impurity scattering in graphene," *Nano Lett.*, vol. 9, no. 4, pp. 1621–1625, 2009.
- [45] F. Chen, Q. Qing, J. Xia, J. Li, and N. Tao, "Electrochemical gate-controlled charge transport in graphene in ionic liquid and aqueous solution," J. Amer. Chem. Soc., vol. 131, no. 29, pp. 9908–9909, 2009.
- [46] X. Dong, Y. Shi, W. Huang, P. Chen, and L.-J. Li, "Electrical detection of dna hybridization with single-base specificity using transistors based on cvd-grown graphene sheets," *Adv. Mater.*, vol. 22, no. 14, pp. 1649–1653, 2010.
- [47] I. M. Sobol, "Global sensitivity indices for nonlinear mathematical models and their monte carlo estimates," *Math. Comput. Simul.*, vol. 55, no. 1-3, pp. 271–280, 2001.
- [48] I. M. Sobol, "Sensitivity estimates for nonlinear mathematical models," Math. Modelling Comput. Exp., vol. 1, no. 4, pp. 407–414, 1993.



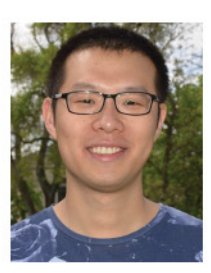
Chao Wang received the B.S. degree in mechanical engineering from the Hefei University of Technology, Hefei, China, in 2012, the M.S. degree in mechanical engineering from the University of Science and Technology of China, Hefei, China, in 2015, and the M.S. degree in statistics and the Ph.D. degree in industrial and systems engineering from the University of Wisconsin-Madison, Madison, WI, USA, in 2018 and 2019, respectively. He is currently an Assistant Professor with the Department of Industrial and Systems Engineering, The University of Iowa,

Iowa City, IA, USA. His research interests include statistical modeling, analysis, monitoring and control for complex systems. He is a Member of the INFORMS, IISE, and SME.



Haihui Pu received the Ph.D. degree from the University of Wisconsin-Milwaukee, Milwaukee, WI, USA, in 2015. He is currently a Staff Scientist with The University of Chicago, Chicago, IL, USA. His research interests include first principles or molecular dynamics simulation and statistical thermodynamics modeling on novel two-dimensional nanomaterials for environmental and energy applications. These include field-effect transistor nanosensors for detecting various targets of interest, such as, gases, heavy metal ions, bacteria, proteins, and viruses, and energy

storage devices, such as, electrochemical fuel cells and batteries.



Xiaoyu Sui received the bachelor's and master's degrees in materialogy from Tongji University, Shanghai, China. He is currently working toward the Ph.D. degree with the Pritzker School of Molecular Engineering, The University of Chicago, Chicago, IL, USA. His research interests include nanoscale engineering of nanomaterials and additive manufacturing for water sensing and energy storage applications.



Junhong Chen received the Ph.D. degree in mechanical engineering from the University of Minnesota, Minneapolis, MN, USA. He is currently a Crown Family Professor of molecular engineering with the Pritzker School of Molecular Engineering, The University of Chicago, Chicago, IL, USA, and a Lead Water Strategist and a Senior Scientist with Argonne National Laboratory. He was a Postdoctoral Scholar of chemical engineering with California Institute of Technology, Pasadena, CA, USA. His research interests interests include molecular engineering of 2D

nanomaterials, hybrid nanomaterials, chemical and biological sensors, and energy devices.



Shiyu Zhou received the B.S. and M.S. degrees in mechanical engineering from the University of Science and Technology of China, Hefei, China, in 1993 and 1996, respectively, and the master's degree in industrial engineering and the Ph.D. degree in mechanical engineering from the University of Michigan, Ann Arbor, MI, USA, both in 2000. He is the Vilas Distinguished Achievement Professor with the Department of Industrial and Systems Engineering, University of Wisconsin-Madison, Madison, WI, USA. His research interests include data-driven

modeling, monitoring, diagnosis, and prognosis for engineering systems with particular emphasis on manufacturing and after-sales service systems. He has established methods for modeling, analysis, and control of Internet of Things (IoT) enabled smart and connected systems, variation modeling, analysis, and reduction for complex manufacturing processes, and process control methodologies for emerging nanomanufacturing processes. His research also attracted significant interest and funding support from several large corporations. He is currently the Director of the IoT Systems Research Center, University of Wisconsin-Madison and a Fellow of the IISE, the ASME, and the SME. He was the recipient of the CAREER Award from the National Science Foundation, the Best Application Paper Award from IIE Transactions, and many highly competitive federal research grants.